Accuracy Evaluation in Robot-Assisted and Ultrasound-Guided Neurosurgery

Pedro Veigas dos Santos
pedro.v.santos@tecnico.ulisboa.pt

Instituto Superior Técnico, Lisboa, Portugal

***Abstract*—The neurosurgery field demands an high level of accuracy and precision associated to each performed procedure. On the other hand, the recent developments in the human-robot area allowed the rise of surgical shared control systems. In these, the surgeon is responsible for every decision, while the robot is responsible for correcting the human error associated do the surgeon's action. In this work a neuronavigation system based on the LBR Med robot, developed by KUKA, is proposed. Furthermore, an error evaluation will be performed to assess the performance of such system, concerning the intra-operative registration and the needle placement stages. By doing so, the most important sources of inaccuracy will be determined. Such evaluation will be performed in the laboratory, in a simulated neurosurgical environment, using an antropomorphic phantom to recreate the patient's cranium and brain. The intraoperative registration will be performed by means of CT and ultrasound images. Thus, the proposed method is a non-invasive one and overcomes the most important drawbacks associated with the state-of-the-art technologies. It is also important to refer that every aspect regarding this stage will be addressed, such as, the ultrasound calibration, the images segmentation and the rigid registration algorithms. Finally, in what concerns the needle positioning, the robot performance will be evaluated using the navigation system Polaris Spectra, developed by Northern Digital.**
Keywords: Neuronavigation, LBR Med, Ultrasound Imaging, Segmentation, Registration

I. Introduction

Throughout the past few decades, a huge effort has been put into the development and improvement of the surgical navigation technology allowing the surgical procedures to be performed in a less invasive manner and still assuring the requirements of high precision and accuracy.

Nowadays, every brain biopsy that employs this methodology follows similar stages. The first, is the acquisition of the preoperative images. Usually both magnetic resonance, MRI, and computed tomography, CT, are used. These allow the surgeon to visualise the patient's brain and to plan the intervention, defining the target location and the best trajectory to reach it.

The second step is the intraoperative image-to-patient registration. In this, a coordinate transformation, that maps every point in the image space to the physical space, is estimated. The techniques available to perform this registration are divided into point-pair matching and surface matching. The first uses a set of fiducials which can be anatomical points of the patient's head, or artificial markers. The second, on its turn, uses the surface of patient's head or cranium, which can be acquired in the physical space using a pointer or a laser scanner.

After the registration is successfully performed, the surgical instruments, tracked by the navigation system, can be seen, in a set of screens, in the image space. This allows the surgeon to move such objects based on the CT-MRI information. Thus, he can use an articulating arm to constrain the probe movement to the trajectory defined in the preoperative stage.

The mean global target errors, of such procedure, have been evaluated by several authors. For instance, there is the work developed in [1], which evaluated three of the most widely used systems: the Medtronic StealthStation, the BrainLab VectorVision and the Voxim from IVS Solutions. This, reported an error ranging from 1-1.5 mm using rigidly attached markers to perform the registration. Furthermore, there is the work developed in [2] which, through a literature review, reported errors ranging from submillimetric to 6 mm. In this work, besides the aforementioned systems, also the FARO Surgicom and the Stryker Nagivation System, among others, were evaluated.

On the other hand, the surgical robotics field has also been getting more attention. Nathoo et al. [3] presents several advantages of using a robotic system in neurosurgery. From those, it is worth stressing the ability to actively constrain the tools to a particular path or position, even against externally imposed forces, the ability to perform repetitive motions and to hold in a specified position for long periods without tremor and the high accuracy and precision that these systems provide.

Therefore, the project presented in this work proposes a robot-assisted neuronavigation system in a shared control fashion, [3], which disregards the use of any additional 3D localization technology in the surgical room. Thus the robot will be used to track the surgical tools and to actively correct the surgeon's action. Furthermore, to overcome the drawbacks associated with the registration methods available, this work uses intraoperative ultrasound imaging to scan the patient's cranium surface in the surgical room.

The use of the aforementioned technologies comes up as a way to perform the neurosurgical procedure in a more accurate, easy and safe manner. Finally, it is the main objective of this work, the evaluation of the system's performance, specially, in what concerns the intraoperative registration and the robot positioning stages.

II. Materials and Methodology

A. Tracking

1) KUKA LBR Med: The LBR Med is a lightweight jointed-arm robot with 7 axes. On their turn, each axis is equipped with a range sensor, a torque sensor and a temperature sensor which are used for control and protective purposes.

Furthermore, in what concerns the robot control modes there are two available: the position, and the impedance control modes. An additional control mode was also implemented. This is the manual guidance mode and it is an impedance control mode with null stiffness.

Finally, the OpenIGTLink communication protocol, [4], was implemented in Java, [5], so to allow the robot to communicate its flange pose to the other devices.

2) Polaris Spectra: The Polaris Spectra, henceforth designated by Polaris, will be used in this work to perform the calibration steps, to perform several measurements used in the accuracy evaluation and to validate the robot positioning. This navigation system provides several tools that can be tracked, which will be attached to important objects whenever it is relevant to measure their positions and orientations. Consequently, these tools will be called trackers throughout this work. Furthermore, there is the stylus. Its tip position can be determined through the pivoting calibration and this will be used to measure the position of static points and surfaces.

B. Imaging

1) CT Scanner: The CT scanner used in this work was the Phillips Brilliance R 64. The scanned image is a volume of 197 slices spaced by 1 mm. Furthermore, each slice has a field of view of 280 mm and consists in a matrix of 512×512 voxels.

2) Aloka ProSound: The device used to acquire ultrasound images was the ProSound 2 and the linear transducer UST-586-5, both developed by Hitachi Aloka. Furthermore, to establish the communication between the ultrasound and the main workstation the frame grabber DFG/USB2propcb was chosen.

C. Tracking and Imaging Fusion

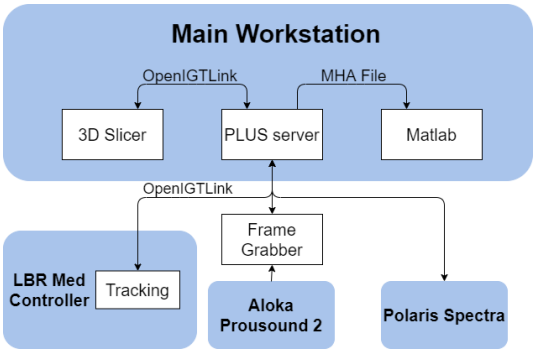

Fig. 1: Devices setup.

Figure 1 shows how every piece of software and hardware is combined together in an experiment. As a summary, important data comes from the robot and the Polaris which are used as trackers to measure poses in space, and from the Ultrasound which sends images through the frame grabber. A PLUS server, [6], is used to synchronize all this information and the 3D Slicer, [7], is used to command the PLUS and to visualize the data through an OpenIGTLink connection. Finally, PLUS saves the important data in a MHA file which is then used by the Matlab where the self-developed algorithms will run. The main workstation used in this work is a computer with an Intel i5-5200U processor running at 2.20 MHz using 6 GB of RAM.

D. Phantom

The main study object in this work is an anthropomorphic phantom based on the human skull with the following dimensions: 305 mm height, 178 mm width and 203 mm length.

Inside the phantom, a group of spheres were placed. These will be used as targets simulating points and paths inside the skull, like tumours for instance. Figure 2 shows the top view of the phantom with the targets spheres placed. These are numbered from 1 to 10 and this numbering will be used throughout this document to indicate each target.

Fig. 2: Phantom top view with numbered targets. (Adapted from [8])

E. Methodology

1) Reference Frames: To start with, it is important to introduce the main reference frames present in this work. In the physical space, the *Polaris*, the robot *Base* and the robot *Flange* are the main ones. Furthermore, there is the *Stylus* and the *Tracker*'s reference frames and the *Ultrasound* frame. The last reference frame present in the physical space is the *Needle* reference frame, of which the Z axis is collinear with the physical needle. Finally, there is the *CT* reference frame which is associated to the image space.

2) Targets: It is through the targets, figure 2, that the performance of the system will be evaluated.

As for the CT space, the position and orientation of each target, defined by p^{CT}_{Target} and v^{CT}_{Target}, were determined using the segmentation capabilities of the 3D Slicer.

On the other hand, in the physical space, each target position, p^{Base}_{Target}, was determined using the stylus. The orientations, v^{Base}_{Target}, on their turn, were determined using the image space orientations. A ground truth coordinate transformation was calculated registering each target position directly and, afterwards, the orientations in the physical space were obtained by transforming the CT space orientations through such transformation.

3) Registration: The registration stage will be performed in a stepwise manner, to evaluate how each source of error affects the final result. Therefore, there are three important point clouds, representing the phantom surface, to be built:

- The CT point cloud, defined by the set of points $p^{CT}_{Phantom}$. This was obtained through an automatic segmentation of the CT volume in Matlab.
- The ultrasound point cloud, defined by the set of points $p^{Base'}_{Phantom}$. The surface of the phantom was imaged using the ultrasound transducer. This was attached to the flange of the robot which was controlled in manual guidance during the process. Each image was automatically segmented in Matlab and the position of each segmented pixel was determined relatively to the robot base reference frame.
- The ground truth point cloud, defined by the set of points $p^{Base}_{Phantom}$. This was acquired with the stylus by sliding its tip over the phantom surface. Each position acquired was then transformed to the base reference frame.

Notice that both the ultrasound and the ground truth point clouds define the phantom surface relative to the robot base frame. For that reason, they should be coincident. However, due to several sources of inaccuracy, the two point clouds will not overlap perfectly. Therefore, to distinguish these, one will assume that the ultrasound point cloud exists in a virtual reference frame, $Base'$.

The registration will then be performed in three steps:

- The first step consists in registering the CT and the ground truth point clouds. The error for this step will be evaluated with equations 1 and 2.

$$e_p = \left\| p^{Base}_{Target} - T^{Base}_{CT} \cdot p^{CT}_{Target} \right\| \tag{1}$$

$$e_v = cos^{-1}\left(v^{Base}_{Target} \cdot (T^{Base}_{CT} \cdot v^{CT}_{Target}) \right) \tag{2}$$

- The second step consists in registering the ultrasound and the ground truth point clouds. The error for this step will be evaluated through equations 3 and 4.

$$e_p = \left\| p^{Base}_{Target} - T^{Base'}_{Base} \cdot p^{Base}_{Target} \right\| \tag{3}$$

$$e_v = cos^{-1}\left(v^{Base}_{Target} \cdot (T^{Base'}_{Base} \cdot v^{Base}_{Target}) \right) \tag{4}$$

- The third and main step is to register the CT and the ultrasound point clouds. This will be evaluated using the equations 5 and 6.

$$e_p = \left\| p^{Base}_{Target} - T^{Base'}_{CT} \cdot p^{CT}_{Target} \right\| \tag{5}$$

$$e_v = cos^{-1}\left(v^{Base}_{Target} \cdot (T^{Base'}_{CT} \cdot v^{CT}_{Target}) \right) \tag{6}$$

Finally, every step that requires the ultrasound images acquisition was performed N times, using independent scans. The performance of the second and third registration steps will, therefore, be evaluated through the mean and standard deviation of each target errors.

4) Needle Placement: Positioning the needle in the physical space means to command the robot to align the Z axis of the needle reference frame with the target orientation. Furthermore, as it is the surgeon's job to push the needle forward until it reaches the target points, a distance d must be kept between the reference frame origin O_{Needle}, and the target position. This is shown in figure 3.

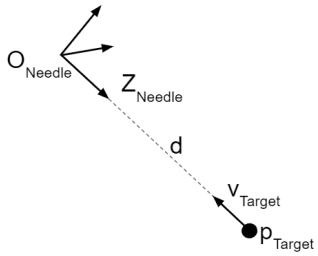

Fig. 3: Needle Placement

The error associated with this stage will be evaluated in two steps:

- In the first step, the robot was commanded to the targets positions acquired by the stylus, in this, no information from the CT image will be used.
- In the second step, the robot was commanded to the positions estimated through the registration between CT and ultrasound point clouds.

The error for both steps will be calculated through equations 7 and 8.

$$e_p = \left\| p^{Polaris}_{Target} - T^{Polaris}_{Tracker} \cdot T^{Tracker}_{Needle} \cdot \begin{bmatrix} 0 \\ 0 \\ d \\ 1 \end{bmatrix} \right\| \tag{7}$$

$$e_v = cos^{-1}\left(v^{Polaris}_{Target} \cdot \left(T^{Polaris}_{Tracker} \cdot T^{Tracker}_{Needle} \cdot \begin{bmatrix} 0 \\ 0 \\ -1 \\ 0 \end{bmatrix} \right) \right) \tag{8}$$

III. Implementation

A. Segmentation

In this section, every image processing technique used to segment the CT and ultrasound images will be described. It is important to mention that segmenting these images means to extract a point cloud that defines the phantom outer surface.

1) CT: As the phantom is defined, in the CT volume, by the voxels with the higher intensities, the first step was the application of a threshold while the second step was to find the voxels which define the phantom outer surface. A searching strategy was implemented to keep only the voxels which define the border of the phantom in each binary axial slice. For each CT slice the rows and columns were searched, and, in each row and column, both directions were covered, i.e., right to left and left to right for rows, and top to bottom and bottom to top for columns, adding up to a total of four loops. Having said so, the first white voxel found in each line or column in each direction was considered to be part of the outer surface.

Finally, the position of each segmented voxel was converted to millimeters and the resulting cloud was downsampled. The result can be seen in figure 4.

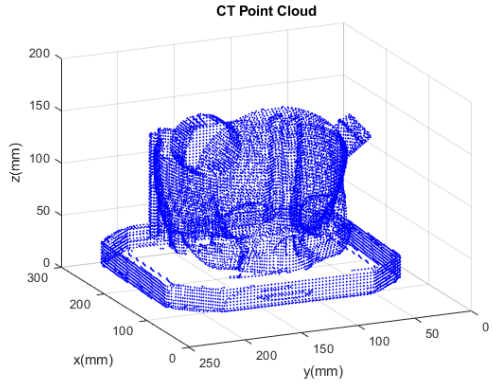

Fig. 4: CT point cloud.

2) Ultrasound: The first step of the ultrasound images segmentation was the application of a Gaussian filter to smooth the imaged surface, and then, a threshold was applied.

Due to the some non-filtered noise, artifacts appear in the binary image. These had to be eliminated to avoid the existence of outliers in the final point cloud. To that end, the connected components in the binary image were determined and only the largest one was kept.

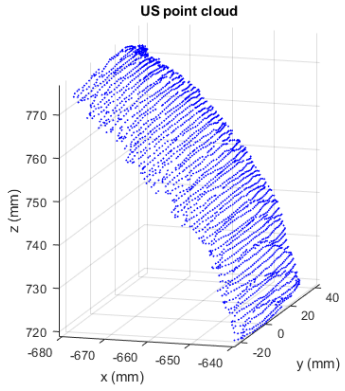

Fig. 5: Phantom forehead point cloud.

To end with, the phantom surface was segmented as the higher pixel in each column. The position of each segmented pixel was converted to millimeters and then transformed to the robot base reference frame. The resulting point cloud was downsampled and the result can be seen in figure 5.

B. Setup Calibration

1) Temporal Calibration: The temporal calibration procedure consists in imaging the bottom of a water tank while performing a sinusoidal movement in the direction perpendicular to the bottom of the tank with the ultrasound probe, [9]. Thus, two sinusoidal signals are built, i.e., the probe movement and the bottom tank position in the ultrasound image. Finally, the time shift can be determined by aligning the two. Figure 6 shows the two sine waves before the calibration and 7 shows the two sine waves after the calibration.

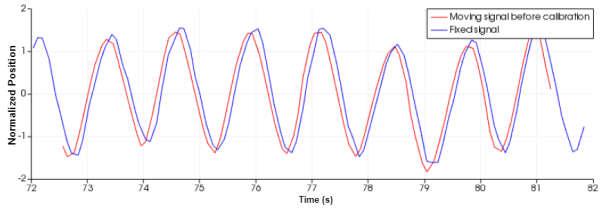

Fig. 6: Sines before calibration.

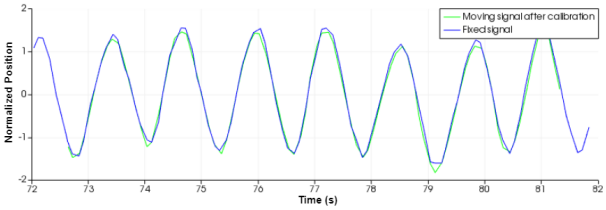

Fig. 7: Sines after calibration.

Since there was the need to synchronize the messages from three devices, the adopted method was to define the ultrasound time delay to be zero and perform the calibration twice. One calibration was performed with the tracking signal coming from the robot and another with the tracking signal coming from the Polaris. Thus, a time delay was computed for the robot messages and a different one was computed for the Polaris messages.

2) Robot-Polaris Calibration: Figure 8 shows the Polaris to robot base calibration setup. The method is divided in two steps, [10]:

- Determining $p_{Flange}^{Tracker}$ through pivoting, similar to the stylus calibration. However, here the robot was commanded to perform the calibration movement automatically.
- Determining $T_{Polaris}^{Base}$ through a point-pair registration. The robot was commanded to move its flange to 150 different positions and a point-pair registration problem was formulated, equation 9.

$$\sum_i \left\| T^{Base}_{Flange,i} \cdot \begin{bmatrix} 0 \\ 0 \\ 0 \\ 1 \end{bmatrix} - T^{Base}_{Polaris} \cdot T^{Polaris}_{Tracker,i} \cdot p^{Tracker}_{Flange} \right\| \tag{9}$$

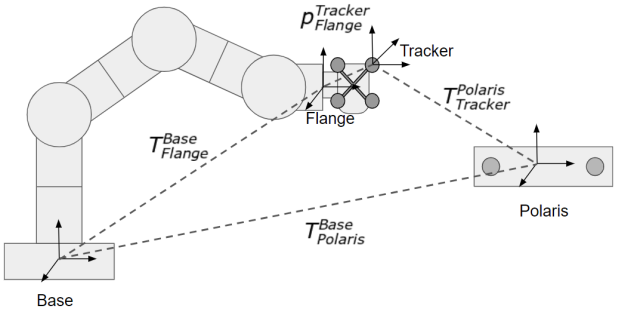

Fig. 8: Calibration setup.

3) Ultrasound Spatial Calibration: The method chosen to perform this step was the stylus-based calibration, [11]. Although, the good precision and accuracy of such method, the misalignment between the stylus and the scan plane is reported as its main source of inaccuracy. Thus, in an attempt to reduce the significance of this issue, this work proposes a new procedure.

The idea behind the attempted solution is to keep the probe still and slowly move the stylus in the direction perpendicular to the scan plane while keeping it parallel to this plane. By moving the stylus this way, in and out of the scan plane, it is possible to assure that at some point it will be perfectly aligned with the plane. It is, then, needed to find a criteria to choose the frame that captured the best alignment.

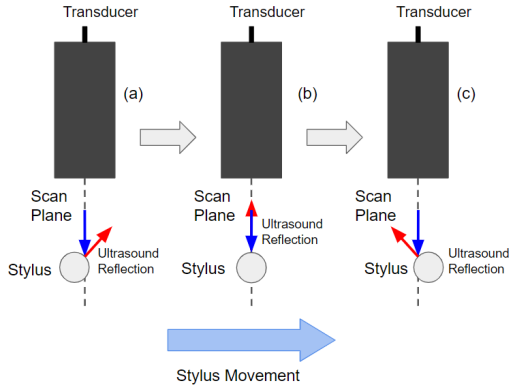

Fig. 9: Stylus movement.

Figure 9 shows, in a simplified manner, what happens when the stylus is moved the described way. In this figure, the blue arrow represents the ultrasound wave emitted by the probe and the red arrow represents the ultrasound wave after being reflected.

It is possible to conclude, by looking at the image, that it is in (b), i.e., when the stylus is the most aligned with the scan plan, that the transducer will receive the greater amount of reflected wave. For that reason, in (b) the stylus will appear much brighter, and thus, the images total intensity is a suitable criteria to choose the right frame.

Finally, the tip of the stylus was segmented in each selected frame. The process of finding the stylus tip in the image is divided into segmenting the stylus and then extracting the tip position. Segmenting the stylus is similar to what was described in for the phantom surface segmentation, i.e., the image was filtered with a gaussian filter, a threshold was applied and the largest connected component was kept. Then, the tip was selected as the segmented pixel in the lowest row or as the mean among the segmented pixels in the lowest row. Figure 10 shows the output of the described procedure.

Fig. 10: Stylus tip segmented.

The position of the pixel was, then, converted to millimeters and a point-pair registration problem was formulated, equation 10.

$$\sum_i \left\| p^{Flange}_{Tip,i} - T^{Flange}_{Ultrasound} p^{Ultrasound}_{Tip,i} \right\| \tag{10}$$

4) Needle Calibration: This was performed as shown in figure 11. A calibrating tool was built, allowing a Polaris tracker to be mounted on one end, and with an hole on the other so to slide it along the needle. The tip, highlighted in the figure, is placed in the center of such hole in the outermost surface of the tool and its position, p^{Tool}_{Tip}, was determined using the stylus. By sliding the tool along the physical needle, a set of points was acquired and an optimization problem was formulated. Note that, since the needle is not completely stiff, it deflects during the process. Thus, the calibration can not be performed with a simple linear regression.

The points acquired with the calibrating tool can be transformed to the needle reference frame through equation 11 or 12, whether one desires to estimate the transformation between the needle and the tracker, or the transformation between the needle and the flange frames of reference.

$$\begin{bmatrix} x_{Needle} \\ y_{Needle} \\ z_{Needle} \\ 1 \end{bmatrix} = T'^{Needle}_{Tracker} \cdot T^{Tracker}_{Polaris} \cdot T^{Polaris}_{Tool} \cdot p^{Tool}_{Tip} \tag{11}$$

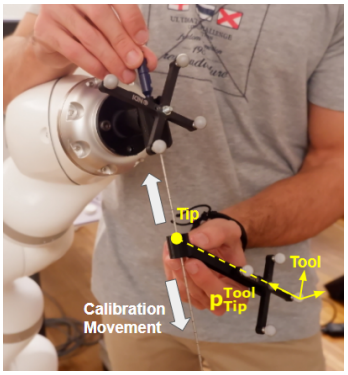

Fig. 11: Needle calibration.

$$\begin{bmatrix} x_{Needle} \\ y_{Needle} \\ z_{Needle} \\ 1 \end{bmatrix} = T'^{Needle}_{Flange} \cdot T^{Flange}_{Base} \cdot T^{Base}_{Polaris} \cdot T^{Polaris}_{Tool} \cdot p^{Tool}_{Tip} \quad (12)$$

Note that both x_{Needle} and y_{Needle} should be equal to zero. Also, the transformations $T'^{Needle}_{Tracker}$ and T'^{Needle}_{Flange} only constrain the Z axis. Therefore these are defined by: a rotation θ_x, a rotation θ_y, a translation d_x and a translation d_y. The cost function for such optimization problem can be built as shown in equation 13.

$$J = \sum_i \left(x^2_{Needle,i} + y^2_{Needle,i} \right) \quad (13)$$

The frame origin position was determined through a simple procedure. The sliding motion begins with the tool tip touching the needle holder surface. So, after the optimization is concluded, the translation d_z is determined so that the origin is coincident with the first points acquired.

C. Registration

In this work two different approaches were attempted. The first approach consisted in performing an initial coarse alignment using the Principal Component Analysis (PCA), [12], [13], followed by a fine registration step with the ICP algorithm, [14]. On the other hand, in the second approach, an iterative algorithm was developed to register the clouds based on the local Gauss and mean curvatures.

It is important to refer that only in the third step of the stepwise registration, described in the *Methodology* section, will the performance associated to the algorithms be evaluated.

Throughout this section, when point clouds are used, as example, for the registration procedure, these will be called fixed and moved such that the estimated transformation is the one that registers the moved point cloud to the fixed point cloud.

1) PCA + ICP Registration: The first step to perform, in this approach, is to calculate a coarse alignment based on the principal components of each point cloud. These can be determined through the eigenvalue decomposition of its covariance matrix. Consider the data set S, a point cloud of n points, of the form 14, and its mean centered form B given by equation 15, where $\bar{S}$ is the mean matrix of S. The principal components of S are the eigenvectors of C, given by 16.

$$S = \begin{bmatrix} s_1 \\ s_2 \\ \vdots \\ s_n \end{bmatrix} = \begin{bmatrix} x_1 & y_1 & z_1 \\ x_2 & y_2 & z_2 \\ \vdots & \vdots & \vdots \\ x_n & y_n & z_n \end{bmatrix} \quad (14)$$

$$B = S - \bar{S} \quad (15)$$

$$C = B^T \cdot B \quad (16)$$

Consider now a fixed point cloud, F, constituted by the points f_i, and a moved point cloud, M, constituted by the points m_i, of the form of 14. Also, each point f_i is determined by applying a rigid coordinate transformation to each point m_i, equation 17. Let V_F and V_M be the principal components matrices of the fixed and moved point clouds respectively.

$$f_i = (R \cdot m_i^T + t)^T \quad \forall \quad f_i \in F \ , \ m_i \in M \quad (17)$$

Which employs:

$$V_F = R \cdot V_M \quad (18)$$

The coordinate transformation that transforms M in F can be calculated following two simple steps. The first is to compute the rotation matrix, R, which can be calculated through equation 19.

$$R = V_F \cdot V_M^T \quad (19)$$

Finally, let $\bar{f}$ and $\bar{m}$ be the the centroids of the fixed and the moved point clouds. The translation vector, t, is given by 20.

$$t = \bar{f}^T - R \cdot \bar{m}^T \quad (20)$$

The second step is the fine tuning of the registration using the ICP algorithm. This, performs the following three steps, in an iterative manner, until a stop criterion is met.

- For each point of the moved point cloud, the correspondent point in the fixed point cloud is the closest one.
- Find the transformation that transforms each point of the moved point cloud to its correspondent point in the fixed point cloud by means of a point-pair registration.
- Apply the estimated transformation to the moved point cloud.

2) Curvature-Based Registration: The first step in the curvature-based registration is the numerical estimation of the mean and the Gauss curvatures of the surface in each point. This is, in turn, divided into estimating the surface normal and the local curvatures, and estimating the principal curvatures, through a least-squares fitting of the Euler curvature equation, for each point, [15]. These are finally used to compute the mean and Gauss curvatures.

The surface normal estimation for each point was performed by means of a principal component analysis of such point neighborhood, [16]. A local cluster was built for each point, constituted by the point itself and its k nearest neighbours. Thus, the principal components of such cluster were determined. The first two principal components will be coplanar to the cluster, while the third can be assumed to be the surface normal in that point.

Then, the local curvatures were also estimated. A new neighborhood for each point P was defined, based on a distance condition. Assume this neighborhood is defined by the set of points Q_i.

Also, let $\{P, X, Y, N\}$ be a local orthogonal coordinate system, as shown in figure 12a.

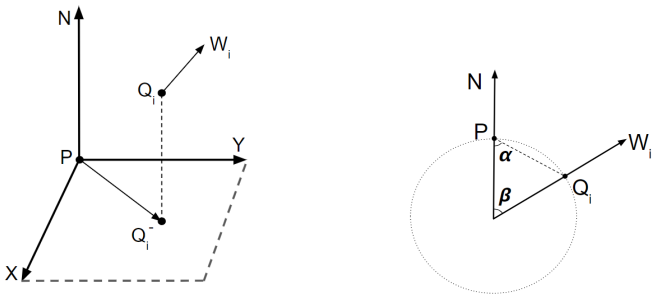

(a) Local coordinate system. (b) 2D curvature.

Fig. 12

In this coordinate system, P is defined by $[0, 0, 0]$ and Q_i by $[x_i, y_i, z_i]$. Also, Q_i^- represents the projection of Q_i in the pane XY and is defined by $[x_i, y_i, 0]$. On the other hand, W_i is the surface normal in the point Q_i and is defined in the local coordinate system by $[w_{x,i}, w_{y,i}, w_{z,i}]$.

Having said so, the problem of computing the local curvatures, k_n^i, is given in 2D as shown in figure 12b, where the the curvature is calculated through equation 21.

$$k_n^i = \frac{sin(\beta)}{\|P - Q_i\| \, sin(\alpha)} \tag{21}$$

Also, for a 3D problem, equation 21 can be approximated by 22.

$$k_n^i = \frac{w_{xy,i}}{\sqrt{x_i^2 + y_i^2} \cdot \sqrt{w_{xy,i}^2 + w_{z,i}^2}} \tag{22}$$

Where:

$$w_{xy} = \frac{w_{x,i} \cdot x_i + w_{y,i} \cdot y_i}{\sqrt{x_i^2 + y_i^2}} \tag{23}$$

Having each local curvature calculated, one can now write the Euler curvature equation as 24 shows.

$$k_n^i = k_1 \; cos^2(\theta_i + \theta) + k_2 \; sin^2(\theta_i + \theta) \tag{24}$$

Where the unknown parameters are θ, k_1 and k_2. By the definition employed, θ is the angle between e_1 and X, and θ_i is the angle between the vector $P\vec{Q}_i^-$ and X.

The optimization problem can finally be formulated, as shown in equation 25, and solved through a least-squares optimization.

$$\underset{k_1,k_2,\theta}{min} \sum_i \left[k_1 \; cos^2(\theta_i + \theta) + k_2 \; sin^2(\theta_i + \theta) - k_n^i\right]^2 \tag{25}$$

The Gauss and mean curvatures were, finally, calculated through 26.

$$K_G = k_1 \cdot k_2 \quad , \quad K_H = \frac{k_1 + k_2}{2} \tag{26}$$

The second step in this method is to apply the registration algorithm itself. In sum, the designed method uses the euclidean distance to define the set of fixed points that can be matched to a moved point, i.e., a given moved point, m_j, can be matched to any fixed point, f_k, such that equation 27 holds.

$$\|m_j - f_k\| < R \tag{27}$$

Then, it uses the estimated curvatures to find the best match within the neighborhood radius R, that is, the point $f_{match,j}$ which is the solution of the equation 28.

$$\underset{f_k}{argmin}(\; |K_G(f_k) - K_G(m_j)| \; + \; |K_H(f_k) - K_H(m_j)| \;) \tag{28}$$

Where $K_G()$ and $K_H()$ define, respectively, the Gauss and mean curvatures of a given point. Finally, a point-pair registration problem is formulated to compute the transformation T_i that best transforms every point m_j to its match. This is shown, in homogeneous coordinates, in equation 29, and the solution can be found through a least-squares optimization.

$$\sum_j \|f_{match,j} - T_i \cdot m_j\| \tag{29}$$

At the end of each iteration, this transformation is applied to the moved point cloud, changing the position of every point m_j, and the value of R is decreased, using equation 30. In this, C is an arbitrary small constant, R_0 is the initial value of R, R_{min} is the minimum allowed value of R and i is the iteration.

$$R_i = max(R_0 \cdot e^{-C \cdot (i-1)} \; , R_{min}) \tag{30}$$

This procedure works under the assumption that the point $f_{match,j}$, that represents the best match to the point m_j, is in its vicinity. However, two things may happen that cause this to not be the case.

In the first iteration the moved cloud is in a random position relative to the fixed cloud. In this case, the aforementioned assumption is obviously wrong. For that reason, in the first iteration, the best match to every moved point is searched through the entire fixed cloud neglecting the distance condition of equation 27. This, however, leads to the second problem.

The estimated curvature for the same theoretical point in the CT point cloud and in the ultrasound point cloud may differ.

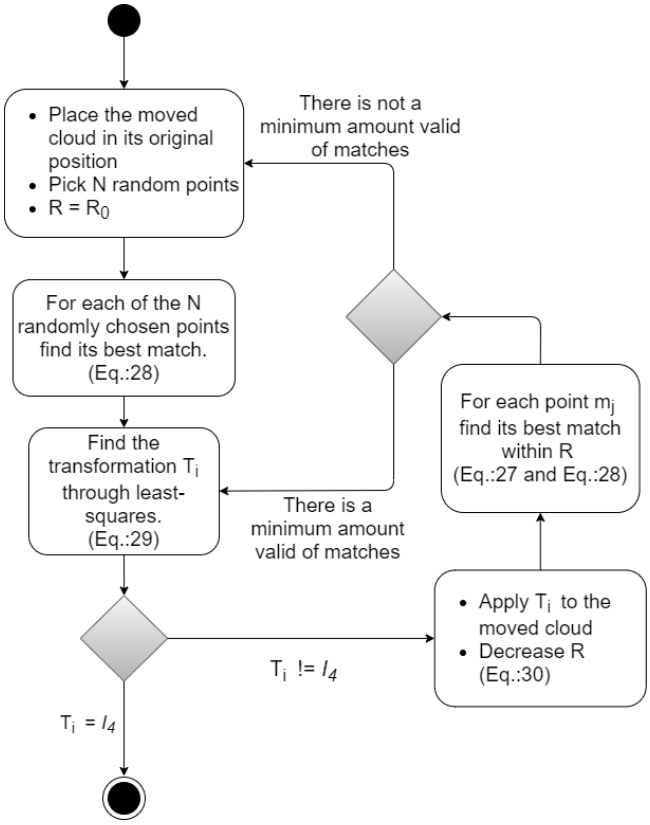

Fig. 13: Registration Algorithm.

Consequently, solving equation 28 with no neighborhood radius condition may result in a wrong matching which leads to a wrong alignment.

When the moved point cloud is transformed with a wrong coordinate transformation, at some iteration, some of the moved points will not have any fixed point in its vicinity, causing the algorithm to get stuck.

For this reason, the first iteration is only performed through N randomly chosen points and, whenever the algorithm gets stuck, the moved points with no neighbours within R are neglected. However, this is done only as long as there is a minimum amount of valid matches. When this minimum is not achieved, it is assumed that the N points chosen for the first iteration failed to give a suitable alignment. Thus the algorithm will restart, placing the moved point cloud in its original position and picking a new set of N initial points. This process is shown schematically in figure 13.

IV. Results and Discussion

A. Calibration

1) Results: Starting by the setup calibration procedure, the first important result is associated to the stylus calibration. This was performed 5 times and the result with the lowest mean residue was kept. The mean stylus calibration residue obtained was 0.42 mm.

The second important calibration result, regarding the Polaris to robot calibration, is the residue of the least squares optimization of the equation 9. The mean residue obtained was 0.40 mm.

The ultrasound spatial calibration was performed 10 times and evaluated through the point reconstruction accuracy PRA, and through the calibration reproducibility CR, [17]. The first was calculated by estimating the position of the tip of a tracked 3D printed cone. This was imaged near the four corners and the center of the image and the mean error obtained was 0.89 mm. The calibration reproducibility, on its turn, was evaluated through the standard deviation of the image corners and center position estimation. The mean result obtained was 0.54 mm.

Finally, the results concerning the needle calibration. The evaluation of the needle calibration quality was performed by calculating the residues of the cost function, equation 13, at the solution. The mean residue obtained was 0.64 mm.

2) Discussion: The two most important results to discuss here are the Polaris to robot calibration and the ultrasound spatial calibration results. In what concerns the first, additional experiments were performed and the conclusion taken was that the mean residue of 0.4 mm is justified by a slight deflection of the robot coupling base.

On the other hand, the error associated to the ultrasound spatial calibration is justified by two main reasons. To start with, the method assumes that the stylus is always parallel to the scan plane. However, it is impossible to assure an absolutely perfect alignment. The second reason has to do with the stylus tip and its segmentation. The diameter of the stylus tip makes it impossible to find a single pixel which corresponds to it with no uncertainty.

B. Registration

1) Results: The first step of the registration stage consists in the CT to ground truth registration. The results for this can be seen in table I.

Target	e_p (mm)	e_v (°)
1	0,69	0,14
2	0,49	0,15
3	0,93	0,19
4	0,62	0,16
5	1,16	0,09
6	0,82	0,19
7	0,74	0,15
8	0,87	0,14
9	0,85	0,10
10	1,30	0,10
Mean	0,85	0,14

TABLE I: CT to ground truth registration error.

To perform the second and third steps of the stepwise error evaluation described in *Methodology* section, 10 different ultrasound scans were made. The results for ultrasound to ground truth registration can be seen in table II.

The third step was then performed. The first attempt to perform this used the PCA + ICP method. The results are presented in table III.

The curvature-based algorithm was, then, applied to solve the CT to ultrasound registration. The results are shown in table IV.

Target	e_p (mm)		e_v (°)	
	Mean	Std. Dev.	Mean	Std. Dev.
2	0,62	0,14	0,42	0,20
3	0,67	0,15	0,40	0,19
4	0,75	0,19	0,40	0,20
5	0,62	0,19	0,37	0,17
6	0,76	0,25	0,4	0,19
7	0,77	0,23	0,42	0,20
8	0,57	0,20	0,42	0,20
9	0,67	0,24	0,39	0,18
10	0,52	0,20	0,40	0,19
Mean	0,66	0,15	0,40	0,19

TABLE II: Ultrasound to ground truth registration accuracy.

Target	e_p (mm)		e_v (°)	
	Mean	Std. Dev.	Mean	Std. Dev.
1	3,12	0,45	4,99	1,07
2	4,43	1,04	4,98	1,06
3	5,44	1,63	5,21	0,95
4	7,28	1,38	3,73	1,00
5	3,28	0,88	4,97	1,11
6	6,04	1,04	5,14	0,90
7	6,81	1,22	4,84	1,06
8	2,45	0,80	5,17	0,97
9	2,32	0,58	4,60	1,19
10	3,44	0,78	5,10	1,02
Mean	4,46	0,73	4,87	1,00

TABLE III: PCA + ICP registration accuracy.

Target	e_p (mm)		e_v (°)	
	Mean	Std. Dev.	Mean	Std. Dev.
1	1,07	0,30	0,76	0,57
2	1,20	0,44	0,76	0,56
3	1,36	0,55	0,78	0,45
4	1,43	0,48	0,79	0,46
5	1,68	0,39	0,78	0,53
6	1,35	0,47	0,77	0,46
7	1,35	0,39	0,78	0,55
8	1,27	0,43	0,76	0,53
9	1,16	0,47	0,79	0,53
10	1,37	0,31	0,79	0,46
Mean	1,32	0,21	0,78	0,50

TABLE IV: Curvature-based registration accuracy.

Finally, the processing time was calculated for every algorithm involved in the registration stage. The results are shown in table V. For the ultrasound segmentation, the time presented is the total time that the algorithm took to segment all the images acquired, while the time present for the registration algorithms is the total time that these took to converge.

Experiment	Processing Time (s)		
	US segmentation	PCA + ICP	Curvature-Based
1	23,64	1,25	33,37
2	23,38	1,72	35,73
3	17,32	0,90	42,96
4	22,27	1,53	45,39
5	19,16	1,80	28,50
6	17,98	1,08	28,76
7	25,48	4,93	29,46
8	26,47	1,28	33,10
9	19,73	1,30	51,66
10	24,61	0,83	29,71
Mean	22,04	1,66	35,86

TABLE V: Processing time.

2) Discussion: The results in table I are mainly due to three reasons. First of all, there is the CT resolution which is around 0.5 mm along the X and Y axes and 1 mm along Z axis. On the other hand, every position measured with the stylus as a certain uncertainty associated, due to the pivoting calibration result shown in the previous section. Finally, there is the imperfect choice of the CT segmentation threshold.

Regarding the second registration step, table II, the procedure was performed 10 times due to the sensibility of the resulting US point cloud to the phantom surface scanning. The final mean errors for this step have, once more, three principal sources of inaccuracy associated. These are the flawed ultrasound spatial calibration and Polaris to base calibration, both presented and discussed in the previous section, and, as for the CT, the ambiguous choice of the ultrasound segmentation threshold.

By performing the third registration step it was possible to verify that the error added by the algorithm employed can be very significant. It is possible, by comparing the results of tables III and IV, to conclude that the information added by the use of the local curvatures, improved the registration quality a lot.

In what concerns, the processing time of the registration algorithms, the major reason behind the huge difference between the results in table V is that, for the ICP, the Matlab built-in function was used. This means that the time consuming part of the PCA+ICP algorithm was performed by compiled code. Differently, in the curvature-based registration the whole process was performed by interpreted code.

C. Needle Placement

1) Results: The results for the first needle placement experiment can be seen in table VI. It is important to refer that there are no results for the targets 5, 9 and 10 because these were not reachable by the robot in the used layout.

Target	e_p (mm)	e_v (°)
1	0,33	0,11
2	0,94	0,27
3	0,57	0,14
4	1,04	0,40
5	—	—
6	0,45	0,13
7	0,45	0,17
8	0,93	0,19
9	—	—
10	—	—
Mean	0,57	0,17

TABLE VI: Needle placement results using the targets measurement.

Since this experiment was performed in a different day, a new CT to ultrasound registration was performed. The result of the said registration can be seen in table VII.

The robot was finally commanded using the registered CT. The results can be seen in figure VIII.

Target	e_p (mm)	e_v (°)
1	1,72	0,80
2	0,88	0,80
3	0,97	0,65
4	1,41	0,81
5	1,34	0,80
6	1,20	0,68
7	1,15	0,80
8	0,90	0,80
9	1,42	0,81
10	1,18	0,86
Mean	1,19	0,80

TABLE VII: Registration result.

Target	e_p (mm)	e_v (°)
1	1,90	0,94
2	1,47	1,01
3	1,26	0,65
4	2,51	1,19
5	—	—
6	1.88	0,76
7	1,39	0,91
8	0,56	0,84
9	—	—
10	—	—
Mean	1,43	0,91

TABLE VIII: Final needle placement results.

2) Discussion: The most prominent source of error behind the results of table VI is related to the robot coupling base deflection. The robot configuration changes the amount of deflection in the coupling base and thus, calibrating the needle using different robot configurations produced different results. It was verified that the targets which demanded a robot configuration most similar to the one used to calibrate, were the ones that presented the lowest errors.

Regarding the results for the registration presented in table VII, these were obtained using the curvature-based algorithm. There is not further to add about them as the registration was already discussed in the previous section.

Finally in what concerns the results presented in table VIII, the biggest contribution comes, obviously, from the registration outcome. However, it was possible to calculate the robot contribution, by subtracting the registration errors to the needle placement errors, and to verify that, once more, the most significant contribution came from the robot coupling base deflection.

V. Conclusions

Throughout the development of this work, the implementation of a robot-assisted and ultrasound-guided neuronavigation system was studied with regard to the image-to-patient registration and robot positioning. As main achievements, it is worth to stress out the design and implementation of a fast, accurate and automatic setup calibration procedure that can be applied to any system with similar characteristics. Besides, a stepwise error evaluation methododology was presented in this work, which can be used to assess the performance of any robot-assisted and ultrasound-guided neuronavigation system, and, the application of such methodology to the KUKA LBR Med, can be used to guide further developments on this project. Finally, it is also important to refer, that it was possible to achieve a final registration stage quality comparable to the most accurate systems available, using an affordable and non-invasive technology.

It is one's belief that the main developments to allow the system to be implemented in a real surgical environment, are the replacement of the coupling base to avoid non-rigid effects, to study of the CT-MRI registration, accounting this as an additional source of error, and to apply the developed procedure with a setup more similar to a real surgical environment, i.e., using a biological subject, the Mayfield clamp and a realistic relative position between the robot and the subject.

References

[1] E. B. Strong, A. Rafii, B. Holhweg-Majert, S. C. Fuller, and M. C. Metzger. Comparison of 3 Optical Navigation Systems for Computer-Aided Maxillofacial Surgery. *Archives of otolaryngology–head neck surgery 134(10):1080-4*, 2008.

[2] L. Stieglitz, J. Fichtner, R. H. Andres, P. Schucht, A.-K. Krähenbühl, A. Raabe, and J. Beck. The Silent Loss of Neuronavigation Accuracy: A Systematic Retrospective Analysis of Factors Influencing the Mismatch of Frameless Stereotactic Systems in Cranial Neurosurgery. *Neurosurgery 72(5)*, 2013.

[3] N. Nathoo, M. C. Cavuşoğlu, M. A. Vogelbaum, and G. H. Barnett. In Touch with Robotics: Neurosurgery for the Future. *Neurosurgery 56(3):421-33; discussion 421-33*, 2005.

[4] J. Tokuda, G. S. Fischer, X. Papademetris, Z. Yaniv, L. Ibanez, P. Cheng, H. Liu, J. Blevins, J. Arata, A. J. Golby, T. Kapur, S. Pieper, E. C. Burdette, G. Fichtinger, C. M. Tempany, and N. Hata. Openigtlink: an open network protocol for image-guided therapy environment. *International Journal of Medical Robotics and Computer Assisted Surgery 5(4):423-34*, 2009.

[5] J. Oliveira. Robotic Navigation System for Needle Positioning in Neurosurgery. Master's thesis, Instituto Superior Técnico, 2019.

[6] A. Lasso, T. Heffter, A. Rankin, C. Pinter, T. Ungi, and G. Fichtinger. Plus: open-source toolkit for ultrasound-guided intervention systems. *IEEE transactions on bio-medical engineering*, 2011.

[7] S. Pieper, M. Halle, and R. Hikinis. 3D Slicer. *IEEE International Symposium on Biomedical Imaging*, 2004.

[8] M. Elyseu. Registo Intraoperatório com Recurso a Ultrassons em Neurocirurgia. Master's thesis, Instituto Superior Técnico, 2018.

[9] E. M. Moult, A. Lasso, T. Ungi, C. Pinter, M. Welch, and G. Fichtinger. Improved Temporal Calibration of Tracked Ultrasound: An Open-Source Solution. *Journal of Medical Robotics Research 02(04):1-8*, 2017.

[10] S. Tovar-Arriaga, R. Tita, J. C. P. Ortega, E. Gorrostieta-Hurtado, and W. A. Kalender. Development of a robotic FD-CT-guided navigation system for needle placement-preliminary accuracy tests. *International Journal of Medical Robotics and Computer Assisted Surgery 7(2):225-36*, 2011.

[11] P.-W. Hsu, G. M. Greece, R. Prager, N. E. Houghton, and A. H. Gee. Comparison of Freehand 3-D Ultrasound Calibration Techniques Using a Stylus. *Ultrasound in Medicine Biology 34(10):1610-21*, 2008.

[12] R. Echeverria-Chasco, C. Cortes, A. Bertelsen, and J. F. Esnal. Robust CT to US 3D-3D Registration by Using Principal Component Analysis and Kalman Filtering. *International Workshop on Computational Methods and Clinical Applications for Spine Imaging*, 2016.

[13] H. Tian, X. Dang, J. Wang, and D. Wu. Registration method for three-dimensional point cloud in rough and fine registrations based on principal component analysis and iterative closest point algorithm. *Traitement du Signal 34(1-2):57-75*, 2017.

[14] P. J. Besl and N. D. McKay. A Method for Registration of 3-D Shapes. *IEEE Transactions on Pattern Analysis and Machine Intelligence 14(2):239-256*, 1992.

[15] X. Zhang. Curvature estimation of 3d point cloud surfaces through the fitting of normal section curvatures. 2008.

[16] H. Hoppe, T. D. DeRose, T. Duchamp, J. A. McDonald, and W. Stuetzle. Surface reconstruction from unorganized points. *ACM SIGGRAPH Computer Graphics*, 1992.

[17] B. Hallgrímsson and C. W. Sensen. *Advanced Imaging in Biology and Medicine*, chapter 3. Springer, 2009.